Journal of Materials Chemistry A

ROYAL SOCIETY OF CHEMISTRY

PAPER

View Article Online
View Journal | View Issue

Cite this: J. Mater. Chem. A, 2020, 8, 7377

A Janus protein-based nanofabric for trapping polysulfides and stabilizing lithium metal in lithium–sulfur batteries†

Min Chen,[ab] Zhiping Chen,[b] Xuewei Fu*[a] and Wei-Hong Zhong*[a]

The shuttling of polysulfides and uncontrollable growth of lithium dendrites remain the most critical obstacles deteriorating the performance and safety of lithium–sulfur batteries. The separator plays a key role in molecule diffusion and ion transport kinetics; thus, endowing the separator with functions to address the two abovementioned issues is an urgent need. Herein, a protein-based, low-resistance Janus nanofabric is designed and fabricated for simultaneously trapping polysulfides and stabilizing lithium metal. The Janus nanofabric is achieved *via* combining two functional nanofabric layers, a gelatin-coated conductive nanofabric (G@CNF) as a polysulfide-blocking layer and a gelatin nanofabric (G-nanofabric) as an ion-regulating layer, into a heterostructure. The gelatin coating of G@CNF effectively enhances the polysulfide-trapping ability owing to strong gelatin–polysulfide interactions. The G-nanofabric with exceptional wettability, high ionic conductivity (4.9×10^{-3} S cm^{-1}) and a high lithium-ion transference number (0.73) helps stabilize ion deposition and thus suppresses the growth of lithium dendrites. As a result, a Li/Li symmetric cell with the G-nanofabric delivers ultra-long cycle life over 1000 h with very stable performance. Benefiting from the synergistic effect of the two functional layers of the Janus nanofabric, the resulting Li–S batteries demonstrate excellent capacity, rate performance and cycling stability (*e.g.* initial discharge capacity of 890 mA h g^{-1} with a decay rate of 0.117% up to 300 cycles at 0.5 A g^{-1}).

Received 19th February 2020
Accepted 22nd March 2020

DOI: 10.1039/d0ta01989e

rsc.li/materials-a

Introduction

With the ever-increasing demand for advanced energy storage systems, numerous efforts have been made to develop electrochemical storage devices including rechargeable batteries, supercapacitors, fuel cells, *etc.* Among these devices, supercapacitors have high power density, but their energy density is limited;[1,2] lithium-ion batteries have achieved great commercialization success, yet the theoretical energy limits make them hardly able to support high-demand applications.[3,4] Recently, lithium–sulfur (Li–S) batteries have been attracting extensive attention and research enthusiasm due to their high theoretical energy density (2600 W h kg^{-1}) and the low cost of sulfur, which is a promising candidate for high-energy storage devices with reduced cost.[5,6] However, the practical application of Li–S batteries is still hindered by several intractable challenges from the intrinsic properties and electrochemistry of the active materials. One of the predominant problems is the shuttling of soluble intermediate polysulfides between the sulfur cathode and lithium anode, *i.e.* the shuttle effect, which results in irreversible loss of sulfur active materials, low coulombic efficiency and quick capacity degradation.[7,8] To inhibit the shuttle effect, many strategies have been proposed, including rational design of sulfur host materials (conductive polymers,[9] nano-carbon[10,11] and graphene oxide,[12–15] and metal oxides[16,17]), modification of electrolyte components[18] and employment of solid electrolytes,[19] as well as engineering of separators.[20] These efforts have made significant progress for improving the performance of the batteries; however, the growth of Li dendrites remains another critical issue in Li–S batteries, which may severely shorten the cycle life, and the growing dendrites may penetrate through the separator, resulting in an internal short-circuit and even explosion and fires.

Besides the studies for resolving the shuttle effect, stabilizing Li metal becomes increasingly important today to realize a high-performance and safe Li–S battery. To achieve that, researchers have attempted various methods such as optimization of electrolyte components,[21,22] creation of an artificial solid electrolyte interphase (SEI),[23,24] introduction of 3D scaffolds,[25,26] and modification of separators. It is known that the nonuniform deposition of Li ions is the factor initiating the formation of lithium dendrites.[27,28] The separator, as a key interfacial component linking the S cathode and Li anode, plays

[a]School of Mechanical and Materials Engineering, Washington State University, Pullman, WA 99164, USA. E-mail: Xuewei.fu@wsu.edu; katie_zhong@wsu.edu
[b]College of Materials Science and Engineering, Chongqing University, 174 Shazhengjie, Chongqing, 400044, China

† Electronic supplementary information (ESI) available. See DOI: 10.1039/d0ta01989e

a crucial role in molecule diffusion and ion-deposition kinetics. Therefore, it is expected that engineering of separators has great potential to synchronously address the two critical issues, the shuttle effect and dendritic Li growth, leading to an improvement in battery performance and safety.

Intensive research has endowed separators with the ability of capturing polysulfides and/or suppressing the growth of Li dendrites. To reduce the shuttle effect, the modified separators or interlayers are supposed to be able to strongly trap polysulfides and to be electrically conductive, thus leading to reduced polysulfide diffusion and improved sulfur utilization.[29] Thus far, various materials that can anchor polysulfides and electrically conductive materials have been employed to fabricate interlayers, including polar polymer functionalized carbon materials,[30] metal oxide/carbon composites,[31] metal oxide/metal nitride heterostructures,[32] conductive metal–organic frameworks (MOFs),[33,34] *etc.* Specifically, due to the vast variety of polar groups, biomaterials have also been applied to trap polysulfides recently, including various polysaccharides (gum arabic,[35] chitosan,[36] *etc.*) and proteins (gelatin,[37] soy protein,[38] *etc.*), which has been summarized in a previous study.[39] Meanwhile, with the aim of stabilizing Li metal, efforts have been primarily concentrated on creating an ion-flux redistributor on the separator, such as N-/S-doped graphene nanosheets (NSG),[40] boron-nitride (BN) nanosheets,[41] $LiNO_3/Al_2O_3$/PVDF,[42] XC72 carbon black interlayer,[43] *etc.* Impressively, some separators modified with a functional layer on both surfaces are able to simultaneously prohibit the shuttling of polysulfides and growth of Li dendrites. In this strategy, polypyrrole,[44] carbon nanotubes,[45] *etc.* have been adopted on both sides of the separators, which not only prevented the migration of polysulfides but also guided uniform Li ion flux. Although the dual-layer functionalized separators were effective in tackling the two critical issues in Li–S batteries, the substantial increase of thickness/mass arising from the added functional layers on the separator inevitably increased the ion-transport resistance and even sacrificed the battery energy density. Therefore, to overcome this issue, design of advanced and dual-functional separators with low ion-transport resistance is strongly needed.

Based on the above considerations, instead of fabricating dual-layer functionalized separators, creation of Janus separators represents a feasible and appealing configuration. The Janus configuration consisting of two parallel functional materials avoids the addition of two functional layers to a conventional separator, thus reducing the ion-transport resistance. For example, Kong *et al.*[46] reported a Janus separator with a carbon nanofiber (CNF) layer toward the sulfur cathode and a polyimide (PI) nanofabric toward the Li metal anode, which could trap and convert polysulfides, and promote Li^+ transport. The polyvinylpyrrolidone (PVP) coated-CNF has dipole–dipole interaction with polysulfides, while the excellent wettability with electrolyte and the highly porous structure of PI nanofibers ensure fast ion transport. A Janus cation exchange membrane consisting of an ultrathin ion-selective dense layer and a microporous supporting layer was fabricated with sulfonated poly(ether ether ketone) (SPEEK), which could effectively sieve the ions with low resistance for Li^+ transfer.[47] In spite of the progress, the inability of these Janus separators for stabilizing Li metal remains a critical drawback, limiting further improvement in the long-term performance of the resulting batteries.

To address the above issue, herein, we report a protein-based, low-resistance Janus nanofabric separator capable of trapping polysulfides and stabilizing Li metal. The Janus nanofabric is fabricated *via* incorporating a gelatin-functionalized conductive nanofabric as a polysulfide-blocking layer, and a gelatin nanofabric as a low-resistance ion-flux regulator into an asymmetric configuration. The conductive nanofabric functionalized by gelatin shows good polysulfide-trapping ability due to gelatin's strong interaction with polysulfides; the gelatin nanofabric shows exceptional wettability, high ionic conductivity and a high Li-ion transference number (0.73), therefore enabling homogenization of the Li ion flux and stabilization of Li metal. As a result, the Li/Li symmetrical cell with the gelatin nanofabric yields long cycle life over 1000 h with a fixed capacity of 0.5 mA h cm^{-2}. The Li–S cell with the Janus nanofabric shows excellent C-rate performance and stable cycling performance for 300 cycles at 0.5 A g^{-1} with a low capacity decay rate of 0.117% per cycle.

Results and discussion

Fig. 1a shows a schematic illustration for the fabrication process of the protein-based Janus nanofabric. The Janus nanofabric is composed of a gelatin-coated conductive nanofabric for blocking polysulfides and an insulative gelatin nanofabric for guiding ion deposition. The gelatin nanofabric (G-nanofabric) was fabricated *via* electrospinning of denatured gelatin solution where the pristine gelatin molecule was disrupted into random polypeptide coils with functional groups exposed. The conductive nanofabric (CNF) was derived from coating polypyrrole (Ppy) on polyvinylpyrrolidone (PVP) nanofibers *via* vapor-phase polymerization of the pyrrole monomer.[44] Denatured gelatin solution was then coated on the conductive nanofibers by drop casting to yield gelatin-functionalized CNF (G@CNF). More experimental details can be found in the Experimental section.† As shown in Fig. 1b, Li–S batteries with a conventional separator suffer from the shuttling of polysulfides and uncontrollable growth of Li dendrites. The shuttling of polysulfides not only consumes the S active material but also corrodes the Li metal. Meanwhile, the formation of Li dendrites resulting from the inhomogeneous deposition of Li ions severely threatens the battery safety. By contrast, in an improved Li–S battery, the Janus nanofabric with the G@CNF toward the S cathode and the G-nanofabric toward the Li anode can trap and convert the dissolved polysulfides to restrain the shuttle effect and protect the Li metal simultaneously. Specifically, the gelatin protein on the G@CNF layer can absorb polysulfides while the G-nanofabric layer can regulate and homogenize the Li-ion flux and thus inhibit the growth of Li dendrites, leading to enhanced performance of Li–S batteries.

The FTIR spectra of PVP nanofibers and the polymerized product, PVP/Ppy nanofibers, are shown in Fig. 2a. For the PVP nanofibers, the absorption peak located at around

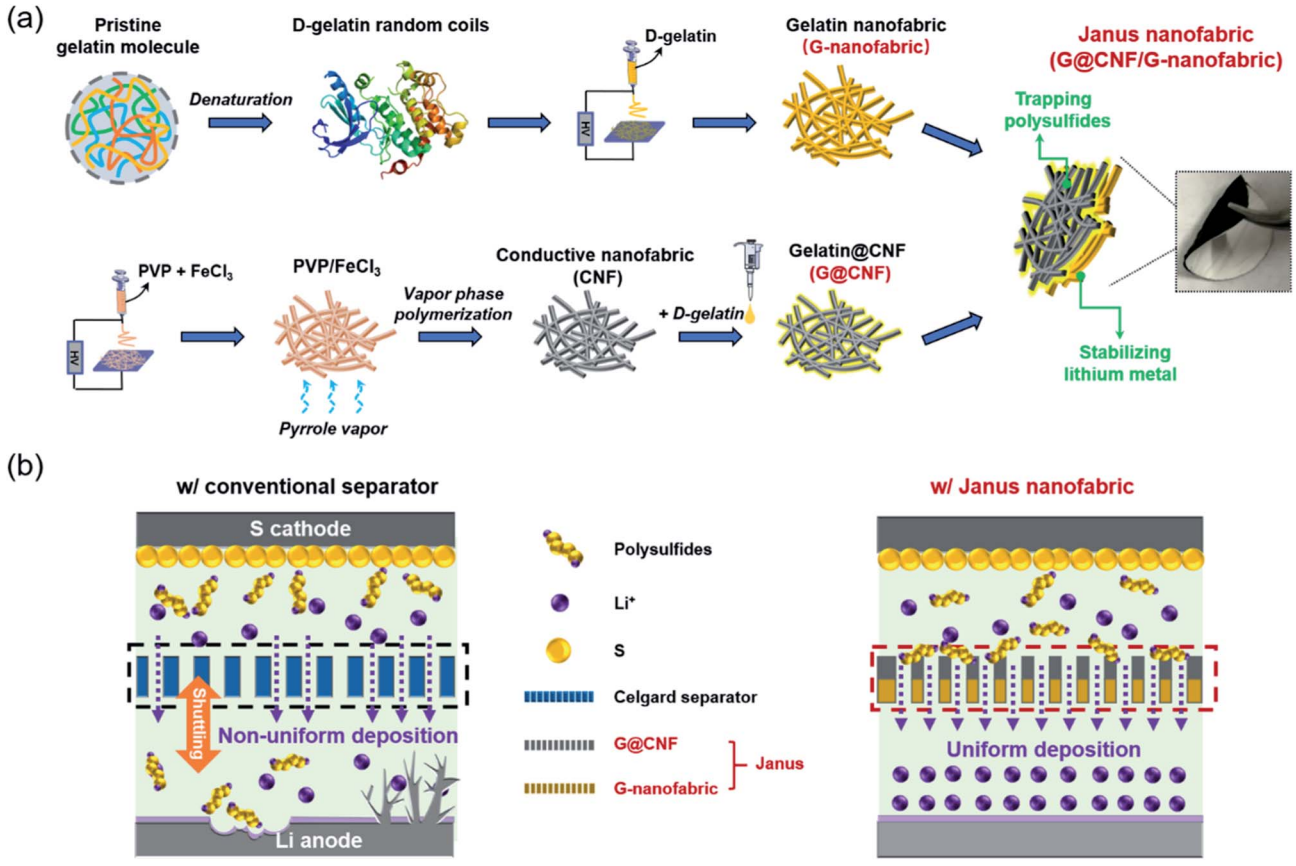

Fig. 1 Fabrication of the protein-based Janus nanofabric and its effect on trapping polysulfides and stabilizing ion deposition. (a) Schematic illustration of the fabrication process of the Janus nanofabric. The Janus nanofabric consists of an upper layer of gelatin-functionalized conductive nanofabric and a lower layer of gelatin nanofabric. (b) Schematic illustration of the contribution from a conventional separator and Janus nanofabric to polysulfide diffusion and Li-ion deposition in Li–S batteries.

1645 cm^{-1} is ascribed to the stretching vibration of C=O, while the C–H bending and CH_2 wagging are observed at 1423 cm^{-1} and 1288 cm^{-1}, respectively. After polymerization, new peaks that are characteristic of polypyrrole appear, including the band at 1554 cm^{-1} corresponding to the ring stretching vibrations of the C=C bond, the band at 1462 cm^{-1} representing the C–N stretching and the N–H in-plane deformation absorption at 1038 cm^{-1}. To endow the nanofabric with electrical conductivity to ensure electrochemical conversion of trapped polysulfides, Ppy was polymerized on the PVP nanofiber surface, and the electrical conductivity varies with the amount of polymerized Ppy. As shown in Fig. 2b, longer reaction time for vapor-phase polymerization leads to generation of more Ppy and thus higher electrical conductivity. After reacting for 26 hours and 40 hours, the electrical conductivities of the resulting nanofibers reach 0.42 and 0.48 S cm^{-1}, respectively. Since the conductivity increase of the PVP nanofibers after 26 hours is not significant, 26 hours was chosen for preparation of conductive nanofibers if it is not specifically noted.

The digital photos and SEM images of the nanofibers at different fabrication stages are shown in Fig. 2c–e. As the morphologies of the nanofabric, *i.e.* fiber diameter and pore size, are critical contributors to the ability of trapping polysulfides, the concentration of the precursor solution for electrospinning was varied from 7 to 9 wt% to tune the fiber morphologies. Fig. S1† shows the diameter distributions of PVP nanofibers obtained from various concentrations of the precursor solutions. The fiber diameter significantly decreases with the solution concentration and 7 wt% yields the thinnest fiber diameter of 236 nm. Likewise, the pore size distribution of the resulting CNF shows a consistent tendency and 7 wt% generates the smallest average pore size of 864 nm (Fig. S2†). Because thinner nanofibers generate higher surface area and surface energy for trapping polysulfides, 7 wt% precursor solution is used for fabricating the PVP nanofabric for the rest of the study. As shown in Fig. 2c, the PVP nanofabric is yellow-colored due to the presence of $FeCl_3$ and has a smooth surface. After polymerization of pyrrole (Fig. 2d), the nanofabric turns black (see the inset) and has a rough surface. Meanwhile, the fiber diameter obviously increases from 236 nm to 286 nm (Fig. 2f and g). These results indicate that the Ppy layer was successfully formed on the fiber surface during the polymerization process with a thickness of about 25 nm. Moreover, the photographs in Fig. S3† indicate that both the PVP nanofabric and CNF have superior flexibility, which make them able to

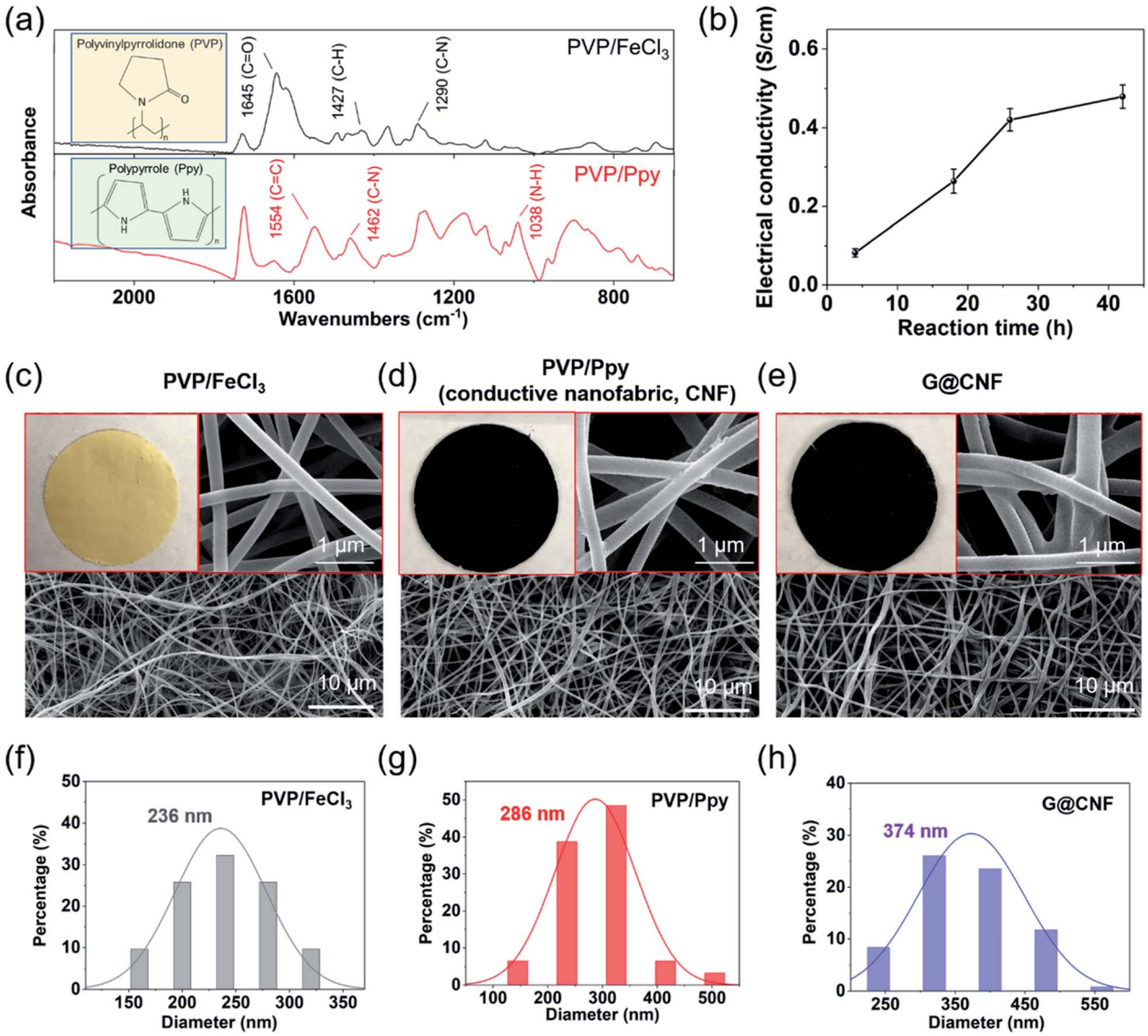

Fig. 2 Morphological study of the gelatin-coated conductive nanofabric. (a) FTIR spectra of PVP and PVP/Ppy nanofabrics. (b) Electrical conductivity of the PVP/Ppy nanofabric as a function of polymerization time. (c–e) SEM images of the (c) PVP nanofabric, (d) PVP/Ppy nanofabric (CNF) and (e) G@CNF. (f–h) Diameter distributions of the (f) PVP nanofabric, (g) PVP/Ppy nanofabric and (h) G@CNF.

withstand severe mechanical deformations. For the G@CNF sample in Fig. 2e, the gelatin coating can be clearly observed on the fiber surface especially at the cross section, and the interconnected fibrous structure is still maintained. The average diameter of G@CNF is about 374 nm compared with that of CNF (286 nm, Fig. 2h), confirming the existence of gelatin coating on the CNF surface with a thickness of ~44 nm.

The G-nanofabric as a multifunctional insulating layer should obtain an appropriate pore structure to feed liquid electrolytes for providing fast ion-conduction pathways. SEM images of the G-nanofabric can be found in Fig. S4,† and they show that the average fiber diameter of the G-nanofabric is ~538 nm. The affinity between the G-nanofabric and electrolytes is characterized by contact angle measurement. A Celgard® separator shows poor wettability to electrolytes with a large contact angle of 72° in the equilibrium state. However, the wettability of the G-nanofabric is excellent and the electrolyte droplet immediately infiltrates the nanofabric within 2 s (Fig. 3a). Moreover, the electrolyte droplet can also quickly penetrate G@CNF (Fig. S5†) resulting in a contact angle of 0°; thus, by combining the G-nanofabric and G@CNF into a Janus nanofabric, superior affinity with liquid electrolytes can be achieved. Besides, the electrolyte uptake of the G-nanofabric is much higher than that of the Celgard® separator. As shown in Fig. 3b, the G-nanofabric shows an extremely high electrolyte uptake of about 700% compared with that of the Celgard® separator (*ca.* 48%). In addition, the G-nanofabric shows a high porosity of 94.9% compared to that of the Celgard® separator (46.8%) (Fig. 3c). Note that the conductive G@CNF layer also shows a high porosity of 79.4%. The high wettability, porosity and electrolyte uptake of the G-nanofabric benefits from the good fibrous structure and the hydrophilic groups from gelatin

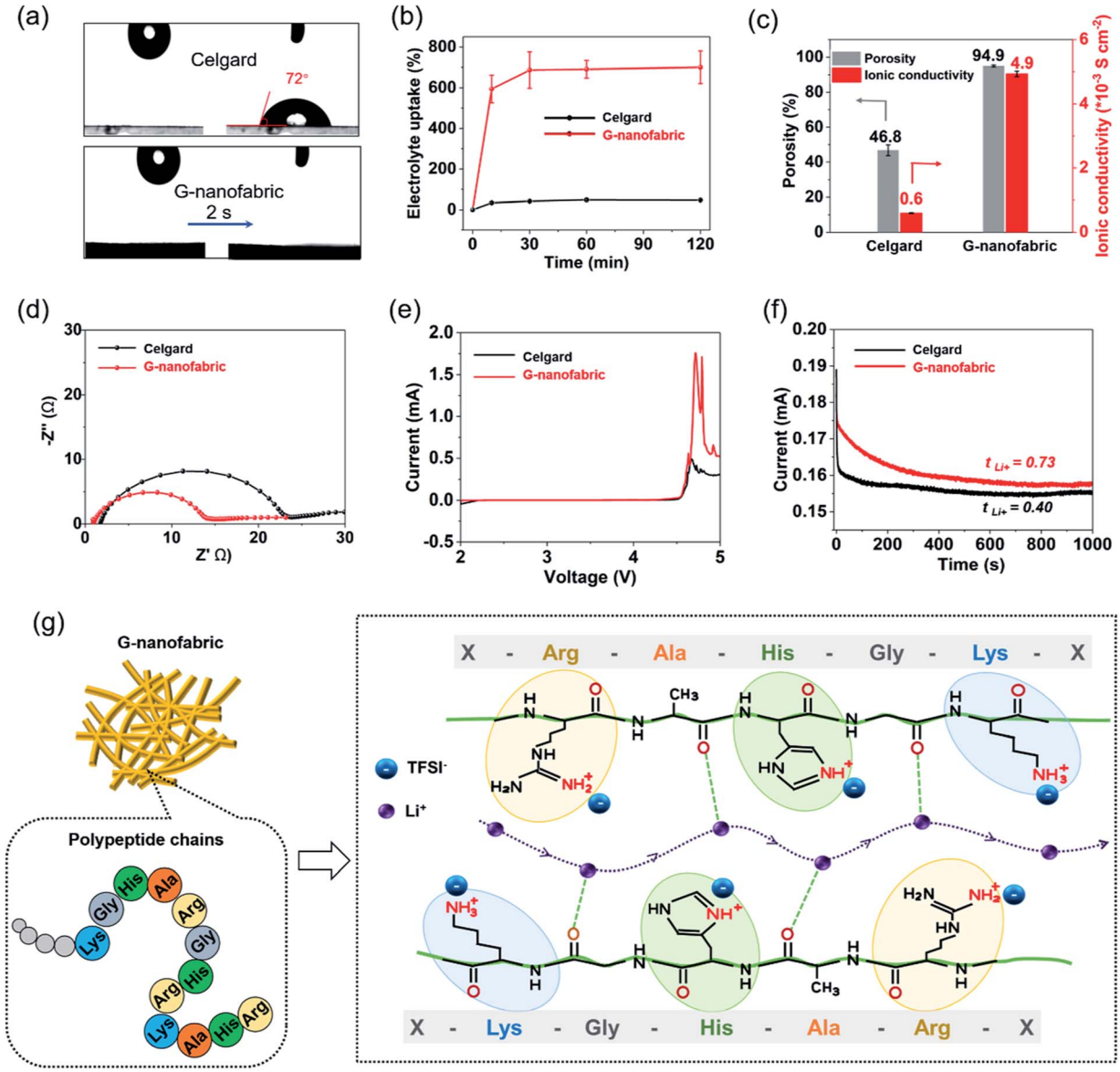

Fig. 3 Electrochemical properties of the G-nanofabric. (a) Contact angle between liquid electrolyte droplets and the G-nanofabric compared with a Celgard® separator. (b) Electrolyte uptake, and (c) porosity and ionic conductivity of the G-nanofabric and Celgard® separator. (d) Nyquist plots showing the comparison of interfacial stability against Li metal in Li/separator/Li cells. (e) Linear sweep voltammetry (LSV) curves of the G-nanofabric and Celgard® separator in Li/separator/stainless steel cells at a scan rate of 0.1 mV s^{-1}. (f) Current response of Li/separator/Li cells under steady state polarization. (g) Schematic illustration of the possible ion-transport situation for the G-nanofabric.

(*e.g.* amine and carboxyl groups; see the FTIR in Fig. S6†), which improves the ion-conducting ability of the G-nanofabric. As shown in Fig. 3c, the ionic conductivity of the G-nanofabric is 4.9×10^{-3} S cm^{-1}, which is about one order of magnitude higher than that of the Celgard® separator (0.6×10^{-3} S cm^{-1}).

Fig. 3d shows the initial interface impedance spectra of Li/separator/Li cells with the G-nanofabric or Celgard® separator. The initial charge-transfer resistance can be obtained from the diameter of the semicircle on the real axis. The resistances for the G-nanofabric and Celgard® separator are 12.7 Ω and 21.8 Ω, respectively, indicating that the G-nanofabric shows better interfacial stability against Li metal. The electrochemical stability is characterized by means of a linear sweep voltammogram (LSV) using a cell of Li/separator/stainless steel (SS). In Fig. 3e, the LSV curves of gelatin and Celgard® are both smooth and steady up to 4.5 V. The abrupt current growth above 4.5 V is due to the decomposition of liquid electrolytes.[48] This result indicates that the G-nanofabric is electrochemically stable up to 4.5 V and can satisfy the potential window for operation of Li–S batteries.

In addition, the Li-ion transference number (t_{Li^+}) is estimated using the Li/separator/Li cell *via* combination measurements of AC impedance and DC polarization, which was originally proposed by Evans and Vincent,[49] and later refined by Abraham and Jiang.[50] Fig. 3f shows the initial and steady current flowing through the cell during polarization under an

applied voltage of 10 mV. The AC impedance before and after polarization can be found in Fig. S7.† The G-nanofabric exhibits a much higher t_{Li^+} of 0.73 than that of the Celgard® separator (0.40). The lone-pair electrons of the nitrogen heteroatoms in proteins can coordinate with Li^+ ions.[51] The complex Li^+ ions will dissociate from their complexation sites and conjugate with new sites, leading to the transfer of Li^+ ions.[24,52] Specifically, from our previous studies,[38] the negatively charged amino acids (Arg, His, and Lys) that attract anions ($TFSI^-$) act as coordination sites, while the backbone oxygens in the gelatin polypeptide chains have good affinity to Li^+, enabling the fast hopping of Li^+ ions between these oxygen atoms, as depicted in Fig. 3g.

Interestingly, it is found that the G-nanofabric is effective in stabilizing Li metal. The Li plating/stripping behavior was first analyzed in Li/Cu cells in which Li was stripped from the Li anode and plated onto a Cu electrode during the discharge process and the process reversed during charging. The contrast in the potential profiles using different separators is shown in Fig. 4a. The complete voltage profiles of the whole 400 h cycling can be found in Fig. S8.† It can be seen that the cell with a Celgard® separator shows gradually increased overpotential upon cycling, demonstrating high resistance for Li nucleation and unstable SEI formation.[53] The unstable SEI results in continuous consumption of Li ions and electrolytes, and eventually failure of the cell after about 380 h. In contrast, the gelatin cell shows a high overpotential in the first three cycles and then the potential hysteresis is decreased and stabilized gradually. This indicates that the deposited Li can be smoothly stripped and a uniform and stable SEI can be formed. The coulombic efficiency of the Li plating/stripping process is shown in Fig. 4b. The gelatin cell shows a high efficiency of about 98.0% in the first 40 cycles, which increases to 99.9% after stabilization. This indicates that the G-nanofabric is able to stabilize Li metal by

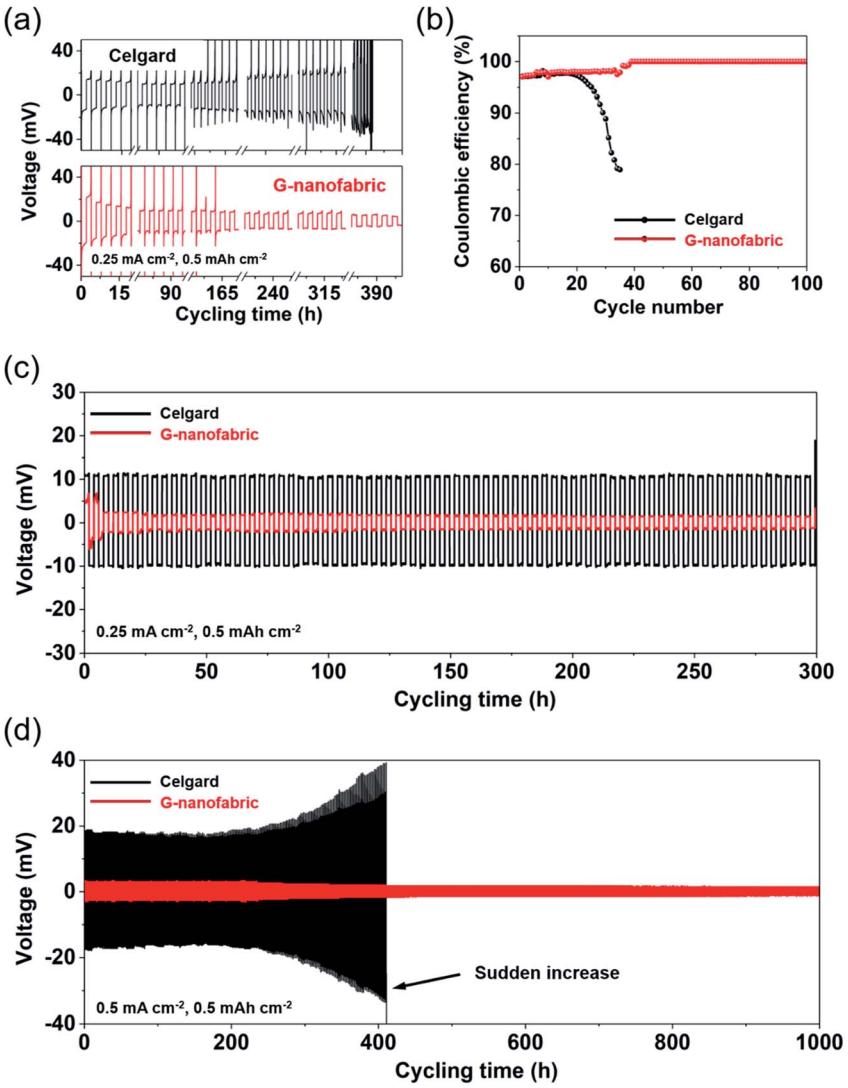

Fig. 4 Li stripping/plating behaviors of the gelatin nanofabric. (a) Voltage profiles of Li/Cu cells during Li stripping/plating cycling at a current density of 0.25 mA cm^{-2}. (b) Coulombic efficiency of the stripping/plating process on the Cu electrode with different separators. (c and d) Voltage profiles of Li/Li symmetric cells at current densities of (c) 0.25 mA cm^{-2} and (d) 0.5 mA cm^{-2}.

forming a thin and stable SEI and Li can be stably and almost completely removed form the Cu electrode in the stripping process. In contrast, the cell with a Celgard® separator exhibits an inferior performance after 20 cycles, with a rapid drop in coulombic efficiency, which results from the formation of Li dendrites and loss of the activated Li metal.[54] The unstable SEI in the Celgard® cell fosters the growth of Li dendrites and induces the isolation of Li particles, causing an irreversible consumption of Li. At a higher current density of 0.5 mA cm^{-2}, the Li/Cu cell with the G-nanofabric maintains low polarization and a long cycle life of more than 600 h (Fig. S9†), confirming that the G-nanofabric is beneficial for stabilizing Li metal.

Moreover, the Li stripping/plating behavior was further studied in Li/Li symmetric cells as shown in Fig. 4c and d. The polarization of the gelatin cell (~3 mV) is significantly lower than that of the Celgard® cell (~10.5 mV) during 300 h of cycling, which implies that the G-nanofabric enables fast and stable deposition of Li^+ ions and helps in the nucleation of Li. At a higher current density of 0.5 mA cm^{-2} (Fig. 4d), the Celgard® cell exhibits rapidly increasing overpotential during cycling and shorts at about 400 h due to the penetration of Li dendrites. The poor performance is due to the unstable deposition of Li^+ ions, which further drives the growth of Li dendrites, and eventually piercing of Li dendrites through the separator. By contrast, the gelatin cell presents an ultra-long lifespan of more than 1000 h with a low and stable overpotential (~2.1 mV). All these results verify that the G-nanofabric can effectively stabilize the deposition of Li^+ ions, leading to a significant improvement in Li stripping/plating performance.

To reveal how the G-nanofabric contributes to stabilizing the ion deposition, the morphology of the post-mortem Li metal was investigated. The morphology of fresh Li metal can be found in Fig. S10,† showing that the surface is flat and smooth. Fig. 5a–d show the morphologies of Li metal after plating or stripping of Li in Li/Li symmetric cells. For the Li metal with the Celgard® separator (Fig. 5a), after depositing Li, considerable nodule-like Li appears resulting in an uneven and rough surface, indicating unstable ion deposition and severe growth of Li dendrites. More seriously, in the stripping process, the unstable SEI layer even cracks, which aggravates the interfacial instability and accelerates the generation of dead Li. The continuous formation/breaking of the SEI layer consumes a large quantity of Li and electrolytes and drives the growth of Li dendrites, which results in increasing overpotential and finally a short-circuit, shown in Fig. 4d. In contrast, the Li metal with the G-nanofabric exhibits a significant morphology change. As shown in Fig. 5c, for both deposited and stripped Li metal, smooth and homogeneous Li is embedded inside the nanofibers, which fills the open space among the individual fibers and even forms a film-like structure. The 3D fibrous structure lowers the local current densities and avoids the formation of "hot spots" by increasing the effective surface area,[55] leading to stable and homogeneous deposition of lithium ions. As a result, the growth of Li dendrites is suppressed, thus resulting in

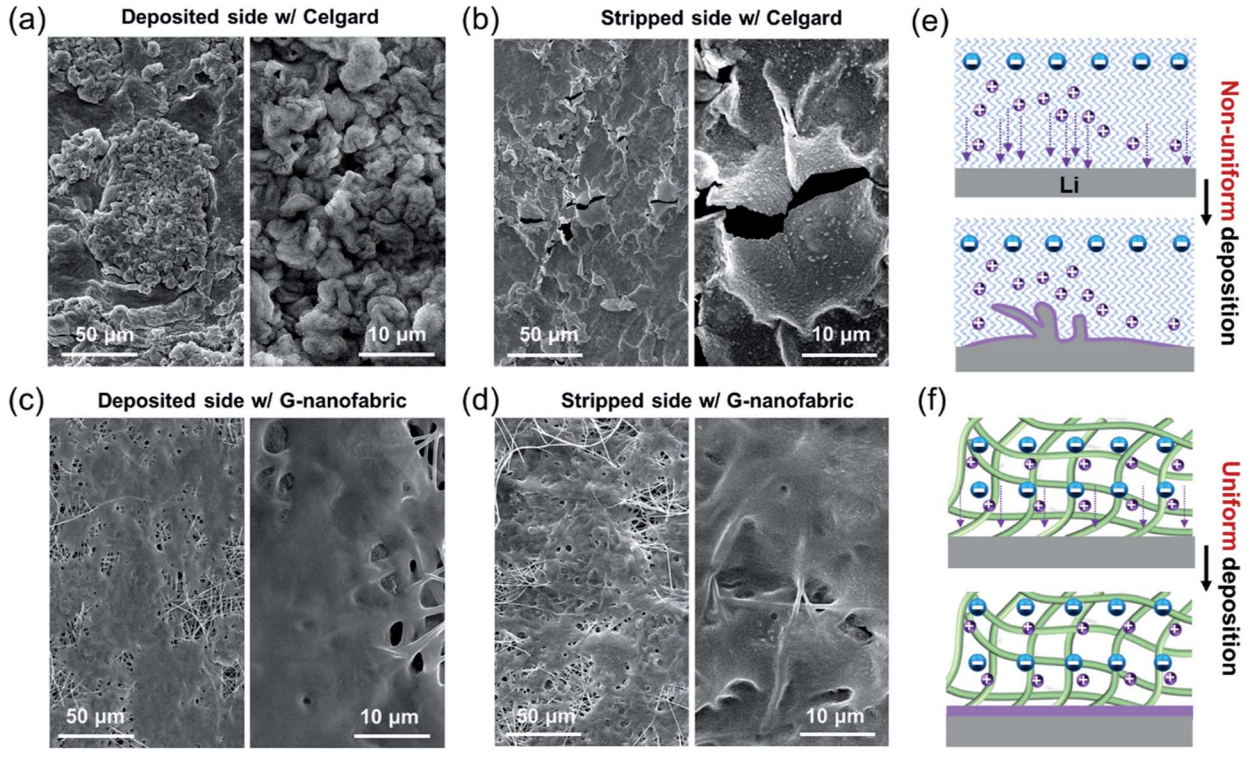

Fig. 5 Morphological study of post-mortem Li metal. (a–d) Morphology of Li metal after 26 cycles of plating or stripping of Li in Li/Li symmetric cells with (a and b) Celgard® and (c and d) the G-nanofabric. (e and f) Schematic illustration of the Li deposition processes with Celgard® or gelatin separators.

exceptional long-term Li plating/stripping performance with stable and low overpotential as discussed above in Fig. 4d.

In addition to the advantages of the 3D fibrous structure of the G-nanofabric in suppressing the dendritic Li growth, the unique electrochemical properties of the G-nanofabric act as additional benefits. As discussed in Fig. 3f, the G-nanofabric exhibits a high Li-ion transference of 0.73, implying that anions can be largely anchored by the nanofabric. As is well known, the "space charge model"[56] attributes the growth of Li dendrites to the depletion of anions in the vicinity of the anode surface. Increasing the Li-ion transference number is believed to be a plausible way of delaying Sand's time (dendrite nucleation time) or stabilizing the electrodeposition.[57] Therefore, as depicted in Fig. 5e, for the cell with a Celgard® separator, the space charge region leads to an inhomogeneous distribution of Li^+ ions, resulting in preferential deposition of Li at relatively sharp tips of the protuberances, which is commonly known as the "tip effect". The concentrated Li^+ ion flux expedites the nucleation and growth of Li metal at some local points, which gradually evolves into Li dendrites.[26] By contrast, the G-nanofabric with a high Li-ion transference number helps prevent the depletion of anions near the Li metal surface in the Li-plating process. As illustrated in Fig. 5f, the G-nanofabric plays two roles here in stabilizing the Li metal: (1) the anions are highly immobilized by the nanofabric, helping to stabilize the electric field and diminish the space charge region; (2) the G-nanofabric with surface polarity has good affinity with Li^+ ions, thus acting as a redistributor for the Li^+ ion flux.[25] As a result, the Li^+ ion flux is homogenized over the entire Li-metal area during cycling and therefore Li-dendrite growth is

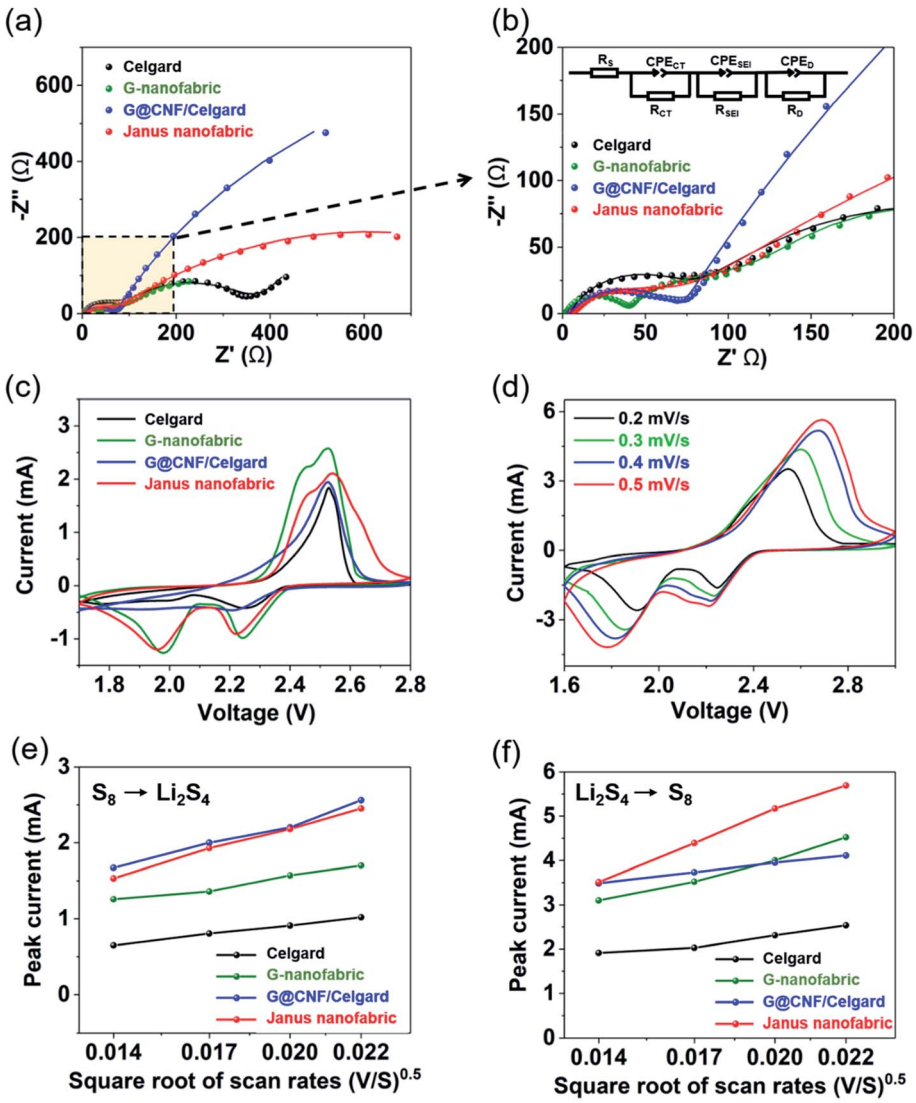

Fig. 6 Electrochemical performance of Li–S batteries with the Janus nanofabric compared with its counterparts. (a and b) Electrochemical impedance spectra of Li–S cells with different separators over a frequency range of 0.01–1 M Hz. The solid lines indicate the fitting results. (c) CV curves of Li–S cells with different separators at a scan rate of 0.1 mV s^{-1}. (d) CV curves of Li–S cells with the Janus nanofabric at different scan rates. (e and f) Plots of CV peak current of (e) the cathodic reaction ($S_8 \rightarrow Li_2S_4$) and (f) the anodic reaction ($Li_2S_4 \rightarrow S_8$) *versus* the square root of scan rates.

suppressed.[58] Finally, planar Li metal embedded inside the fiber matrix is formed as can be seen in Fig. 5c and d. Due to the synergistic effect of the G-nanofabric, the cycle performance of the Li/gelatin/Li cell is far superior to that of the Li/Celgard®/Li cell.

To understand the significant impact of the Janus nanofabric on Li–S cells, electrochemical impedance spectroscopy (EIS) was conducted on the fresh cells in the discharged state. Typical EIS plots with equivalent circuit models are shown in Fig. 6a and b and the electrochemical impedance parameters are summarized in Table S1 (ESI†). The intercepts of the plots on the real axis at high frequency are related to the bulk resistance (R_b). For cells with G@CNF/Celgard® or G@CNF/G-nanofabric (Janus nanofabric), the Nyquist plots are composed of a single semicircle and an inclined line, which correspond to the charge-transfer process (a parallel connection of R_{CT} and CPE_{CT}) and a diffusion process (simulated by R_D// CPE_D),[59] respectively. As for cells with the Celgard® separator or G-nanofabric, there are two sequential semicircles in the high-to-medium frequency region. Besides the one indicating the charge transfer process (in the high frequency region), the other one in the medium frequency region corresponds to interface impedance (a parallel connection of R_{SEI} and CPE_{SEI}) that indicates Li-ion diffusion resistance through the Li_2S/Li_2S_2 solid film.[31] Firstly, regarding the Celgard® separator and G-nanofabric, the R_{CT} (36.8 Ω) of the G-nanofabric is much smaller than that of the Celgard® separator (67.8 Ω) mainly because of the high ionic conductivity of the G-nanofabric. Secondly, compared with the cells without the G@CNF interlayer, the R_{SEI} of G@CNF modified cells, *i.e.* the cells with G@CNF/Celgard® and the Janus nanofabric, is negligible, which suggests that the G@CNF interlayer inhibits the diffusion of dissolved polysulfides from the S cathode side to the Li anode; thus almost no Li_2S/Li_2S_2 solid film forms after the first discharge. To be more specific, the cell with the Janus nanofabric shows a much smaller R_{CT} of 60.9 Ω compared with 66.6 Ω for the G@CNF/Celgard® cell, which benefits from the high ionic conductivity of the G-nanofabric. Interestingly, the R_{SEI} (83.1 Ω) of the cell with only the G-nanofabric is even smaller than half that of the Celgard® (194.9 Ω) cell, which is ascribed to the strong capability of gelatin for trapping polysulfides, although the large pores of the G-nanofabric still allow some diffusion of polysulfides. The EIS results reveal that (1) the G-nanofabric has low charge-transfer resistance and some effect in trapping polysulfides, making it a low-resistance "secondary guard" for blocking the diffusion of polysulfides to the Li anode side; and (2) G@CNF is very effective in trapping polysulfides. Therefore, incorporation of G@CNF and the G-nanofabric into a Janus configuration is beneficial for attaining a low-resistance separator for trapping polysulfides and ensuring fast redox reaction.

Cyclic voltammetry (CV) was performed to study the reaction kinetics of Li–S batteries with different separators. As shown in Fig. 6c, in the cathodic scan the peak at around 2.25 V corresponding to the reduction of S_8 into high-order lithium polysulfides (Li_2S_x, $4 \leq x \leq 8$) can be observed in all cells. It is worth noting that the cells with gelatin or Janus nanofabrics exhibit very dominant peaks and higher peak currents at 1.95 V compared with the cells with Celgard® separators, suggesting that the G-nanofabric enables a fast reduction of soluble lithium polysulfides to insoluble lower-order lithium sulfides (Li_2S_2 or Li_2S). In the oxidation process, one merged peak can be observed in all cells, which suggests that lithium sulfides (Li_2S_2/Li_2S) are converted to soluble lithium polysulfides (Li_2S_x, $4 \leq x \leq 8$) and then finally to S_8. It is found that the cells with gelatin and Janus nanofabrics display two well-defined redox peaks with high peak currents, indicating less polarization and a rapid conversion kinetics.[15]

In order to explore the Li-ion diffusion properties for different separators, CV measurements under different scan rates ranging from 0.2 to 0.5 mV s^{-1} were performed. Fig. 6d shows the CV curves of the cell with the Janus nanofabric at varying scan rates, which demonstrate that the peak current and polarization increase with the scan rate. The current contributed by the redox processes in the bulk part of the separator materials is generated by the directed diffusion of charge carriers, and it is linearly proportional to the square root of the scan rate.[60] Hence, Li-ion diffusion properties can be estimated according to the classical Randles–Sevcik equation[61] and the linear relationship between the peak currents and square root of scan rates can be seen in Fig. 6e and f. The slopes of the curves are positively correlated with the corresponding Li-ion diffusion coefficient. Since the binding of Li_2S/Li_2S_2 with the separator materials is mainly dependent on the two Li atoms, the Li ion diffusion can also indicate the diffusivity of sulfide species on the surface of the separators.[62] During the discharging process in Fig. 6e, the Janus nanofabric has the highest slope or Li-ion diffusion coefficient followed by G@CNF/Celgard®, indicating that the G@CNF layer helps trap and then convert the polysulfides to Li_2S/Li_2S_2, which reduces the viscosity of the electrolyte and prevents the deposition of insulating S-species on electrodes. Meanwhile, the G-nanofabric of the Janus nanofabric greatly benefits the diffusion of Li^+ ions due to its high ionic conductivity. In the charging process (Fig. 6f), the gelatin-containing separators outperform the two groups of cells with Celgard® separators, and the Janus nanofabric shows the highest Li-ion diffusion coefficient. This is possibly because the reduction of Li^+ to Li metal becomes a dominant factor and Li^+ ions diffuse faster with the G-nanofabric.

To further reveal the advantages of the Janus nanofabric, the electrochemical performances of Li–S batteries with different separators were compared. The untreated conductive nanofabric interlayer with a smaller diameter delivers higher discharge capacity due to its higher surface area, as shown in Fig. S11.† Taking a closer look, one can find that the capacity difference between the samples of 7 wt% and 9 wt% decreases with current density, which possibly results from the pore size distribution. As discussed in Fig. S2,† the CNF interlayer obtained from 9 wt% solution has a large pore size and thus shows less resistance to lithium ion transport. Therefore, the inferiority of 9 wt% CNF is reduced at a high current density of 1 A g^{-1}. It has been reported that gelatin protein has strong interaction with polysulfides due to the oxygen atoms in the

backbone,[63] which can be deduced from the cycle performance comparison in Fig. S12† where G@CNF shows higher capacity and slower decay than CNF. As shown in Fig. 7a, the cell with the Janus nanofabric shows the highest initial discharge capacity (1438 mA h g^{-1}) followed by G@CNF/Celgard® (1310 mA h g^{-1}), compared with the conventional G-nanofabric (1295 mA h g^{-1}) and Celgard® separator (978 mA h g^{-1}). Specifically, the Janus nanofabric leads to the greatest utilization of sulfur active materials of as high as 85.9%. These results suggest that the G@CNF layer effectively suppresses the diffusion of polysulfides and the loss of sulfur active materials. Meanwhile, in comparison to the Celgard® separator, the G-nanofabric shows some ability to trap polysulfides as evidenced by the higher capacity than that of the Celgard® separator. The voltage profiles are also compared at a current density of 0.3 A g^{-1} (Fig. S13†), in which the Janus nanofabric shows advantages in terms of high capacity and the G-nanofabric helps reduce the polarization. Fig. 7b plots the specific discharge capacities *versus* different current densities. The cell with the Celgard® separator shows the poorest rate performance with the discharge capacity being as low as 138.9 mA h g^{-1} at a current density of 1 A g^{-1}. Replacing the Celgard® separator with the G-nanofabric, though the capacities at low current densities are similar, the capacity at 1 A g^{-1} is dramatically improved (up to 512.0 mA h g^{-1}), benefiting from the low charge-transfer resistance (Fig. 6a and b). Inserting

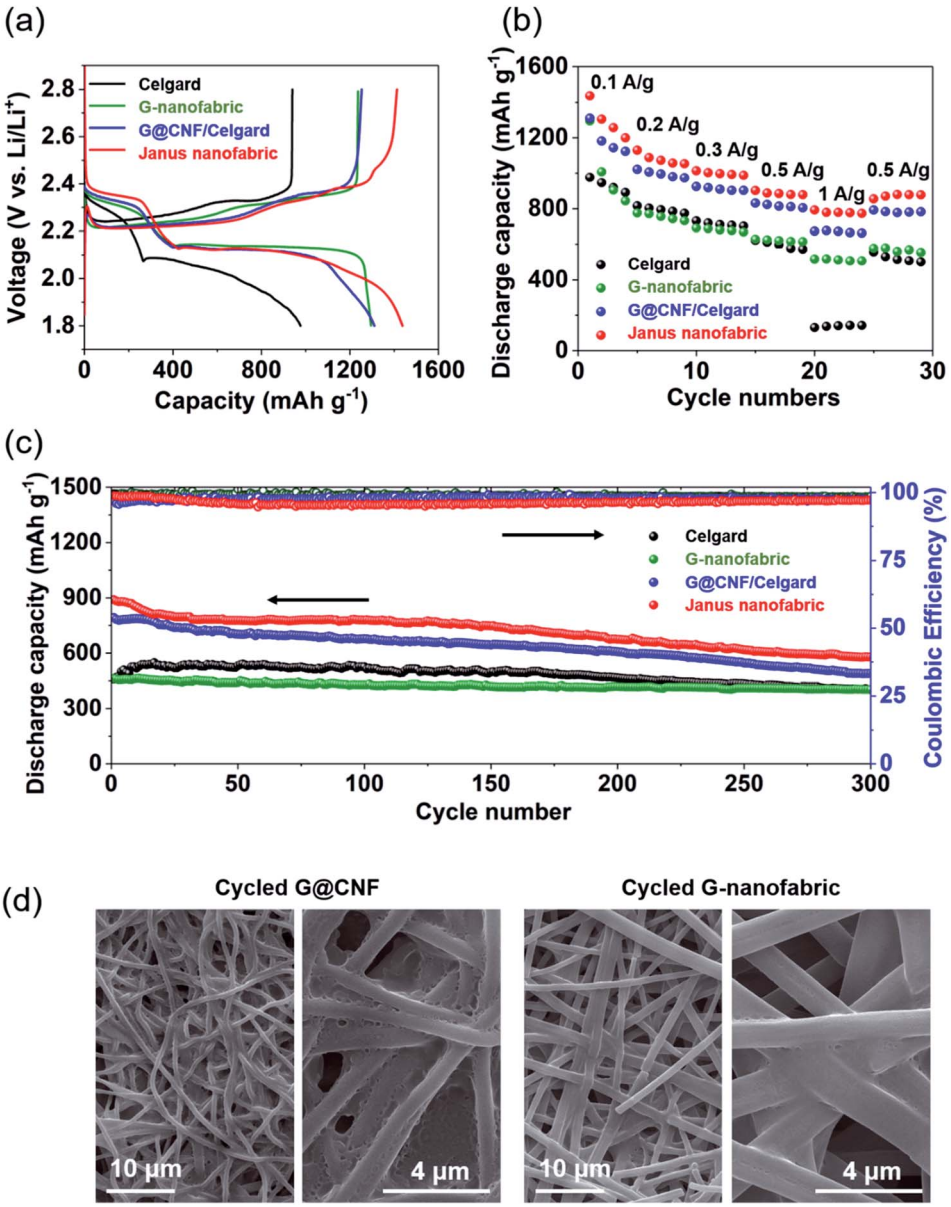

Fig. 7 Charge–discharge performance of Li–S batteries with the Janus nanofabric compared with its counterparts. (a) Charge–discharge profiles of Li–S cells with different separators at 0.1 mA g^{-1}. (b) Rate performances of Li–S cells. (c) Cycling performance of Li–S cells at 0.5 A g^{-1}. (d and e) SEM images of the two layers of Janus nanofabric: (d) G@CNF and (e) G-nanofabric, disassembled from cycled Li–S cells in the discharged state.

a G@CNF layer improves the capacity because of the strong polysulfide-trapping ability and the high electrical conductivity. Besides, the 3D conductive skeleton of the G@CNF layer provides a large surface area for electronic contact with the captured polysulfides and more channels for ionic transfer.[64,65] Therefore, the G@CNF/Celgard® and Janus nanofabric yield much higher capacities than the Celgard® separator or G-nanofabric alone in all current density ranges. Specifically, the Janus nanofabric delivers the highest discharge capacities of 1266, 1040, 970, 883 and 780 mA h g^{-1} at current densities of 0.1, 0.2, 0.3, 0.5 and 1 A g^{-1}, respectively. When the current density is changed back to 0.5 A g^{-1}, the capacity recovers to 872 mA h g^{-1} with a retention of 98.8%. The exceptional rate performance of the Janus nanofabric is the combined result of the low resistance of the G-nanofabric and effective capture-convention of polysulfides by G@CNF, which leads to fast ion-transport, reduced loss of sulfur species, and smooth polysulfide-conversion kinetics. The diffusion experiment results in Fig. S14† verify the polysulfide-trapping capability of the Janus separator. It apparently shows that the Janus separator effectively suppressed the diffusion of polysulfides in the course of the 24 h-diffusion test, as the much lighter color of the electrolyte solution at the bottom indicates a mitigated contamination from the polysulfide diffusion compared with that for the Celgard® separator.

The cycle performance of different separators is compared in Fig. 7c. The pristine Celgard® cell yields an initial discharge capacity of 525 mA h g^{-1} after activation and the capacity decays to 399 mA h g^{-1} after 300 cycles, due to a substantial loss of sulfur active materials and the severe shuttle effect. With the introduction of the G@CNF layer, the G@CNF/Celgard® cell exhibits improved discharge capacity with an initial discharge capacity of 792 mA h g^{-1} and a decay rate of 0.128% per cycle. Compared with the Celgard® separator, the G-nanofabric shows extremely stable cycling capacity and after 300 cycles the capacity retention is as high as 87.4% of the initial capacity. However, the overall capacity is lower than that of the Celgard® separator. As shown in Fig. S15,† the G-nanofabric disassembled from cycled batteries shows severe accumulation of S-species filling the pores due to strong adsorption of polysulfides by gelatin, which blocks the ion-conduction pathways. This results in the low capacity of the cell with the G-nanofabric. More significantly, the Janus nanofabric cell presents the highest capacities throughout the tested cycles. The initial capacity and retention capacity after 300 cycles are 890 mA h g^{-1} and 577 mA h g^{-1}, respectively. The results clearly indicate that the Janus nanofabric effectively inhibits the shuttle effect and ensures sufficient redox reactions. Despite the coulombic efficiency of the Janus separator being relatively low, the effectiveness in suppressing the shuttle effect can be justified for two reasons. First, the capacities of the cells with the Janus separator and G@CNF/Celgard® are much higher than those of the cells without G@CNF, which indicates that polysulfides are massively blocked and re-utilized by G@CNF. The lower coulombic efficiencies of these two cells are mainly caused by the mitigated diffusion of polysulfides gradually occurring over cycling, in contrast to the cells without G@CNF where sulfur is promptly consumed and becomes a sacrificed species, thus showing higher coulombic efficiencies. Second, in comparison with the pristine Celgard® separator, the cell with the G@CNF/Celgard® separator shows a comparable coulombic efficiency, while the Janus separator shows a slightly inferior efficiency. This suggests that G@CNF is effective in suppressing the shuttle effect, but the large pores (average pore size: *ca.* 1.65 μm) of the G-nanofabric (see Fig. S4c†) may result in a loss of sulfur species. By refining the morphologies of the G-nanofabric, the performance of the Janus separator is anticipated to be further improved.

The SEM images of two layers, G@CNF and G-nanofabric, of cycled Janus nanofabrics are shown in Fig. 7d. Compared with fresh G@CNF in Fig. 2e, the cycled G@CNF is covered by S-species resulting in the formation of a film-like structure, which confirms the ability of G@CNF to capture polysulfides. By contrast, the cycled G-nanofabric still maintains its fibrous structure, although some S-species accumulates along the fibers. This suggests that polysulfides are greatly adsorbed by the G@CNF layer. Thus, only a few polysulfides diffuse to the G-nanofabric layer, which can be captured by the G-nanofabric serving as the "secondary guard". The foremost advantage of the Janus configuration is the capability of suppressing both the shuttle effect and dendrite growth without creating redundant layers. However, the thickness of the Janus separator is ~35 μm, which needs to be further reduced to meet the requirements of practical applications. With processing technologies being refined and structural control of the nanofabrics being optimized, a further reduction of thickness and mass is expected.

Conclusion

In summary, we report a protein-based, low-resistance Janus nanofabric capable of capturing polysulfides and stabilizing lithium metal simultaneously. The Janus nanofabric is fabricated *via* incorporation of a gelatin-functionalized conductive nanofabric as a polysulfide-trapping layer, and a gelatin nanofabric as a low-resistance ion-regulating layer into an asymmetric configuration. The conductive nanofabric boosted by gelatin coating demonstrates good ability to trap polysulfides due to gelatin's chemisorption of polysulfides. The gelatin nanofabric shows excellent electrolyte uptake (700%), high ionic conductivity (4.9×10^{-3} S cm^{-1}) and a high Li-ion transference number (0.73), making it effective in stabilizing ion deposition. As a result, the symmetric Li/Li cells with the gelatin nanofabric yield ultra-long cycle life over 1000 h and stable cycling performance. Benefiting from the synergistic effect of the two functional layers, the resulting Janus nanofabric demonstrates low ion-transport resistance and excellent capability for both trapping polysulfides and suppressing dendritic Li growth. Upon incorporating the Janus nanofabric into Li–S batteries, the rate performance, capacity and cycling stability are significantly enhanced (*e.g.* initial discharge capacity of 890 mA h g^{-1} with a decay rate of 0.117% up to 300 cycles at 0.5 A g^{-1}). This work provides an instructive and flexible strategy for the development of multi-functional separators *via*

combining constituents with rationally designed properties for high-power battery systems.

Conflicts of interest

There are no conflicts to declare.

Acknowledgements

This work was supported by NSF CBET 1929236. Ms Min Chen was sponsored by the China Scholarship Council for her visit to Washington State University. The authors would like to gratefully acknowledge the support for microscopy characterization from the Franceschi Microscopy & Imaging Center at Washington State University.

References

1 A. Borenstein, O. Hanna, R. Attias, S. Luski, T. Brousse and D. Aurbach, *J. Mater. Chem. A*, 2017, **5**, 12653–12672.
2 M. Liu, B. Li, H. Zhou, C. Chen, Y. Liu and T. Liu, *Chem. Commun.*, 2017, **53**, 2810–2813.
3 H. Lee, M. Yanilmaz, O. Toprakci, K. Fu and X. W. Zhang, *Energy Environ. Sci.*, 2014, **7**, 3857–3886.
4 X.-C. Zhao, P. Yang, L.-J. Yang, Y. Cheng, H.-Y. Chen, H. Liu, G. Wang, V. Murugadoss, S. Angaiah and Z. Guo, *ES Materials & Manufacturing*, 2018, **1**, 67–71.
5 X. Fu and W. H. Zhong, *Adv. Energy Mater.*, 2019, **9**, 1901774.
6 H. Yuan, J. Q. Huang, H. J. Peng, M. M. Titirici, R. Xiang, R. Chen, Q. Liu and Q. Zhang, *Adv. Energy Mater.*, 2018, **8**, 1802107.
7 L. Zhang, Y. Wang, Z. Niu and J. Chen, *Carbon*, 2019, **141**, 400–416.
8 Q. Qi, X. Lv, W. Lv and Q.-H. Yang, *J. Energy Chem.*, 2019, **39**, 88–100.
9 W. Li, Q. Zhang, G. Zheng, Z. W. Seh, H. Yao and Y. Cui, *Nano Lett.*, 2013, **13**, 5534–5540.
10 G. Hu, C. Xu, Z. Sun, S. Wang, H. M. Cheng, F. Li and W. Ren, *Adv. Mater.*, 2016, **28**, 1603–1609.
11 S. H. Chung, C. H. Chang and A. Manthiram, *Energy Environ. Sci.*, 2016, **9**, 3188–3200.
12 M. Liu, Q. Meng, Z. Yang, X. Zhao and T. Liu, *Chem. Commun.*, 2018, **54**, 5090–5093.
13 M. Liu, Y. Liu, Y. Yan, F. Wang, J. Liu and T. Liu, *Chem. Commun.*, 2017, **53**, 9097–9100.
14 Y. Liu, Y. Yan, K. Li, Y. Yu, Q. Wang and M. Liu, *Chem. Commun.*, 2019, **55**, 1084–1087.
15 M. Liu, Z. Yang, H. Sun, C. Lai, X. Zhao, H. Peng and T. Liu, *Nano Res.*, 2016, **9**, 3735–3746.
16 X. Liang, C. Hart, Q. Pang, A. Garsuch, T. Weiss and L. F. Nazar, *Nat. Commun.*, 2015, **6**, 5682.
17 Z. Z. Yang, H. Y. Wang, L. Lun, W. Cheng, X. B. Zhong, J. G. Wang and Q. C. Jiang, *Sci. Rep.*, 2016, **6**, 22990.
18 J. Zheng, X. Fan, G. Ji, H. Wang, S. Hou, K. C. DeMella, S. R. Raghavan, J. Wang, K. Xu and C. Wang, *Nano energy*, 2018, **50**, 431–440.
19 Y. Lu, X. Huang, Z. Song, K. Rui, Q. Wang, S. Gu, J. Yang, T. Xiu, M. E. Badding and Z. Wen, *Energy Storage Mater.*, 2018, **15**, 282–290.
20 Y. Jeong, J. Kim, S. Kwon, J. Oh, J. Park, Y. Jung, S. Lee, S. Yang and C. Park, *J. Mater. Chem. A*, 2017, **5**, 23909–23918.
21 J. Qian, B. D. Adams, J. Zheng, W. Xu, W. A. Henderson, J. Wang, M. E. Bowden, S. Xu, J. Hu and J. G. Zhang, *Adv. Funct. Mater.*, 2016, **26**, 7094–7102.
22 W. Li, H. Yao, K. Yan, G. Zheng, Z. Liang, Y.-M. Chiang and Y. Cui, *Nat. Commun.*, 2015, **6**, 7436.
23 N. W. Li, Y. X. Yin, C. P. Yang and Y. G. Guo, *Adv. Mater.*, 2016, **28**, 1853–1858.
24 Y. X. Tang, J. Y. Deng, W. L. Li, O. I. Malyi, Y. Y. Zhang, X. R. Zhou, S. W. Pan, J. Q. Wei, Y. R. Cai, Z. Chen and X. D. Chen, *Adv. Mater.*, 2017, **29**, 1701828.
25 Z. Liang, G. Zheng, C. Liu, N. Liu, W. Li, K. Yan, H. Yao, P.-C. Hsu, S. Chu and Y. Cui, *Nano Lett.*, 2015, **15**, 2910–2916.
26 X. B. Cheng, T. Z. Hou, R. Zhang, H. J. Peng, C. Z. Zhao, J. Q. Huang and Q. Zhang, *Adv. Mater.*, 2016, **28**, 2888–2895.
27 J. Xiao, *Science*, 2019, **366**, 426–427.
28 D. Lin, Y. Liu and Y. Cui, *Nat. Nanotechnol.*, 2017, **12**, 194.
29 Y. C. Jeong, J. H. Kim, S. Nam, R. P. Chong and S. J. Yang, *Adv. Funct. Mater.*, 2018, **28**, 1707411.
30 X. Fu, Y. Wang, L. Scudiero and W.-H. Zhong, *Energy Storage Mater.*, 2018, **15**, 447–457.
31 W. Kong, L. Yan, Y. Luo, D. Wang, K. Jiang, Q. Li, S. Fan and J. Wang, *Adv. Funct. Mater.*, 2017, **27**, 1606663.
32 J.-L. Yang, S.-X. Zhao, Y.-M. Lu, X.-T. Zeng, W. Lv and G.-Z. Cao, *Nano Energy*, 2020, **68**, 104356.
33 Y. Zang, F. Pei, J. Huang, Z. Fu, G. Xu and X. Fang, *Adv. Energy Mater.*, 2018, **8**, 1802052.
34 S. Bai, X. Liu, K. Zhu, S. Wu and H. Zhou, *Nat. Energy*, 2016, **1**, 16094.
35 S. Tu, X. Chen, X. Zhao, M. Cheng, P. Xiong, Y. He, Q. Zhang and Y. Xu, *Adv. Mater.*, 2018, **30**, 1804581.
36 H. M. Kim, H.-H. Sun, I. Belharouak, A. Manthiram and Y.-K. Sun, *ACS Energy Lett.*, 2016, **1**, 136–141.
37 M. Chen, X. Fu, N. D. Taylor, Z. Chen and W.-H. Zhong, *ACS Sustainable Chem. Eng.*, 2019, **7**, 15267–15277.
38 X. Fu, L. Scudiero and W.-H. Zhong, *J. Mater. Chem. A*, 2019, **7**, 1835–1848.
39 M. Chen, C. Li, X. Fu, W. Wei, X. Fan, A. Hattori, Z. Chen, J. Liu and W.-H. Zhong, *Adv. Energy Mater.*, 2020, **10**, 1903642.
40 W.-K. Shin, A. G. Kannan and D.-W. Kim, *ACS Appl. Mater. Interfaces*, 2015, **7**, 23700–23707.
41 W. Luo, L. Zhou, K. Fu, Z. Yang, J. Wan, M. Manno, Y. Yao, H. Zhu, B. Yang and L. Hu, *Nano Lett.*, 2015, **15**, 6149–6154.
42 Y. Guan, A. Wang, S. Liu, Q. Li, W. Wang and Y. Huang, *J. Alloys Compd.*, 2018, **765**, 544–550.
43 Y. Ye, L. Wang, L. Guan, F. Wu, J. Qian, T. Zhao, X. Zhang, Y. Xing, J. Shi and L. Li, *Energy Storage Mater.*, 2017, **9**, 126–133.
44 Y. Li, W. Wang, X. Liu, E. Mao, M. Wang, G. Li, L. Fu, Z. Li, A. Y. S. Eng, Z. W. Seh and Y. Sun, *Energy Storage Mater.*, 2019, **23**, 261–268.

45 K. Xie, K. Yuan, K. Zhang, C. Shen, W. Lv, X. Liu, J.-G. Wang and B. Wei, *ACS Appl. Mater. Interfaces*, 2017, **9**, 4605–4613.
46 L. Kong, X. Fu, X. Fan, Y. Wang, S. Qi, D. Wu, G. Tian and W.-H. Zhong, *Nanoscale*, 2019, **11**, 18090.
47 Z. Li, Y. Han, J. Wei, W. Wang, T. Cao, S. Xu and Z. Xu, *ACS Appl. Mater. Interfaces*, 2017, **9**, 44776–44781.
48 C. Ding, X. Fu, H. Li, J. Yang, J. L. Lan, Y. Yu, W. H. Zhong and X. Yang, *Adv. Funct. Mater.*, 2019, **29**, 1904547.
49 J. Evans, C. A. Vincent and P. G. Bruce, *Polymer*, 1987, **28**, 2324–2328.
50 K. Abraham, Z. Jiang and B. Carroll, *Chem. Mater.*, 1997, **9**, 1978–1988.
51 H. Wu, Q. Wu, F. Chu, J. Hu, Y. Cui, C. Yin and C. Li, *J. Power Sources*, 2019, **419**, 72–81.
52 J. Liu, Q. Zhang, T. Zhang, J. T. Li, L. Huang and S. G. Sun, *Adv. Funct. Mater.*, 2015, **25**, 3599–3605.
53 X. Li, S. Guo, H. Deng, K. Jiang, Y. Qiao, M. Ishida and H. Zhou, *J. Mater. Chem. A*, 2018, **6**, 15517–15522.
54 S. J. Zhang, Z. G. Gao, W. W. Wang, Y. Q. Lu, Y. P. Deng, J. H. You, J. T. Li, Y. Zhou, L. Huang and X. D. Zhou, *Small*, 2018, **14**, 1801054.
55 C.-P. Yang, Y.-X. Yin, S.-F. Zhang, N.-W. Li and Y.-G. Guo, *Nat. Commun.*, 2015, **6**, 8058.
56 N. Ohta, K. Takada, L. Zhang, R. Ma, M. Osada and T. Sasaki, *Adv. Mater.*, 2006, **18**, 2226–2229.
57 P. Bai, J. Li, F. R. Brushett and M. Z. Bazant, *Energy Environ. Sci.*, 2016, **9**, 3221–3229.
58 M. H. Ryou, D. J. Lee, J. N. Lee, Y. M. Lee, J. K. Park and J. W. Choi, *Adv. Energy Mater.*, 2012, **2**, 645–650.
59 N. A. Canas, K. Hirose, B. Pascucci, N. Wagner, K. A. Friedrich and R. Hiesgen, *Electrochim. Acta*, 2013, **97**, 42–51.
60 X. Yang and A. L. Rogach, *Adv. Energy Mater.*, 2019, **9**, 1900747.
61 P. Li, L. Shao, P. Wang, X. Zheng, H. Yu, S. Qian, M. Shui, N. Long and J. Shu, *Electrochim. Acta*, 2015, **180**, 120–128.
62 X. Tao, J. Wang, C. Liu, H. Wang, H. Yao, G. Zheng, Z. W. Seh, Q. Cai, W. Li and G. Zhou, *Nat. Commun.*, 2016, **7**, 11203.
63 X. Fu, C. Li, Y. Wang, L. Scudiero, J. Liu and W. H. Zhong, *J. Phys. Chem. Lett.*, 2018, **9**, 2450–2459.
64 M. Liu, P. Zhang, Z. Qu, Y. Yan, C. Lai, T. Liu and S. Zhang, *Nat. Commun.*, 2019, **10**, 1–11.
65 B. Li, Y. Yan, C. Shen, Y. Yu, Q. Wang and M. Liu, *Nanoscale*, 2018, **10**, 16217–16230.